compounds

MDPI

Article

Application of the Hirshfeld Atom Refinement to Determine the Spin State of the Novel Fe(III) Schiff Base Complex

Elena A. Buvaylo [1], Dmytro S. Nesterov [2,3], Evgeny Goreshnik [4] and Oksana V. Nesterova [3,*]

[1] Department of Chemistry, Taras Shevchenko National University of Kyiv, 64/13 Volodymyrska Str., 01601 Kyiv, Ukraine; vinograd@univ.kiev.ua
[2] Centro de Química Estrutural, Institute of Molecular Sciences, Departamento de Engenharia Química, Instituto Superior Técnico, Universidade de Lisboa, Av. Rovisco Pais, 1049-001 Lisboa, Portugal; dmytro.nesterov@tecnico.ulisboa.pt
[3] Centro de Estudos de Engenharia Química, Instituto Superior de Engenharia de Lisboa, Instituto Politécnico de Lisboa, R. Conselheiro Emídio Navarro, 1, 1959-007 Lisboa, Portugal
[4] Department of Inorganic Chemistry and Technology, "Jožef Stefan" Institute, Jamova cesta 39, 1000 Ljubljana, Slovenia; evgeny.goreshnik@ijs.si
* Correspondence: oksana.nesterova@vis.isel.pt

Abstract

The novel complex [Fe^{III}(HL)(L)]·2dmf (**1**) was successfully synthesized by reacting iron chloride with dimethylformamide solution of the Schiff base ligand (H_2L). The ligand was prepared in situ through the condensation of 5-bromo-salicylaldehyde and benzhydrazide. The compound **1** was investigated by single crystal X-ray diffraction, IR spectroscopy, CASSCF/NEVPT2 and DFT theoretical calculations, revealing the high-spin (S = 5/2) state of Fe(III). The Hirshfeld Atom Refinement (HAR) of the crystal structure confirmed the sextet ground spin state of **1** through the comparison of R-factors and Hirshfeld deformation maps of the structures refined assuming high, indeterminate (S = 3/2) and low (S = 1/2) ground spin states. A series of basis sets and DFT functionals was screened, indicating that in most cases the combinations allow the correct determination of the ground state of **1**. The def2-SVP double-zeta basis set combined with the GGA (Generalized Gradient Approximation) functional such as PBE or BP86 was found to be a sufficiently precise low-cost computational level. While further investigation is necessary, the results of the work tentatively suggest that the HAR could be successfully used for determination of the ground spin state of Fe(III) complexes even in the case of regular quality X-ray structures.

Keywords: iron complexes; Schiff base ligands; single crystal X-ray crystallography; theoretical calculations; quantum crystallography; Hirshfeld atom refinement; NoSpherA2

Check for updates

Academic Editor: Salah Massoud

Received: 29 June 2026
Revised: 30 July 2026
Accepted: 31 July 2026
Published: 5 August 2026

Copyright: © 2026 by the authors. Licensee MDPI, Basel, Switzerland. This article is an open access article distributed under the terms and conditions of the Creative Commons Attribution (CC BY) license.

1. Introduction

Synthesis and structural investigation of coordination compounds of transition methods is a broad area of modern chemistry. Among them, the complexes of 3d transition metals, including iron, are of special interest due to their variety of properties and potential to replace expensive platinum-group metals in many applications, first of all in catalysis [1–4]. Compounds whose metal centers may exist in several electronic states have even larger sphere of application, being of high attention due to the spin-crossover and related features [5,6]. At the same time, correct determination of a ground spin state of iron or manganese complexes is a challenge [7–9], since common combinations of structural parameters, bond valence calculations and other indirect data may give misleading results.

The Fe(III) cation has $3d^5$ electronic configuration with maximum of five unpaired electrons. While the high-spin (HS) state with $S = 5/2$ is the most common for Fe(III) compounds, depending on the coordination environment the iron center may exist in the intermediate (IS) or low (LS) spin states with $S = 3/2$ and $1/2$, respectively [10,11]. The best methods for determining the spin state of a given Fe(III) compound involve Raman, EPR and Mössbauer spectroscopies, often accompanied by theoretical calculations. However, one of the most common methods in practical chemistry, single crystal X-ray diffraction (SCXRD), is still almost unused for direct determination of oxidation and spin states, where the respective studies are limited to the comparison of M–X bond lengths with the reference values extracted from the structural databases [11,12].

The above limitations of the SCXRD appear from the method of structural refinement called the Independent Atom Model (IAM) [13], which presumes that atoms are isolated in their ground states and thus their scattering functions are fully spherical and do not depend on the chemical environments. While the IAM approach is robust and widespread, being implemented in SHELXL and many other packages, nowadays the reflections data obtained from modern X-ray diffractometers are precise enough to account for much deeper effects of electron density distribution, such as chemical bonds, lone pairs and spin states. The theoretically calculated aspherical scattering factors can be used in Hirshfeld Atom Refinement (HAR), producing much more accurate calculated electron density than that obtained from the classic IAM method [14,15]. With the current development of the respective software, such as the NoSpherA2 program [16] implemented in the Olex2 package, the HAR of the crystal structures becomes a practically accessible and reproducible procedure, as evidenced by remarkable recent studies where the HAR was successfully applied towards characterization of new compounds [17–19].

Despite the progress in the field, there are still very few applications of HAR for direct determination of the spin state of 3d metal complexes. A prominent example is the confirmation of the high-spin state of Fe(II) complexes by quantum crystallography recently reported by Kleemiss and co-workers [20]. Being inspired by those findings, we applied the HAR methodology towards the novel Schiff base Fe(III) complex with the aim of exploring the abilities and limits of the HAR in the present case. Herein we report the synthesis, crystal structure and theoretical studies of the coordination compound $[Fe^{III}(HL)(L)]\cdot 2dmf$ (**1**), for which the ground high-spin state was confirmed by the methods of quantum crystallography. The influence of basis set, DFT functional and other conditions has been studied.

2. Materials and Methods

2.1. General

All reagents were purchased from local suppliers and used as received. The IR spectrum was recorded on a PerkinElmer 1600 FT–IR instrument (PerkinElmer Inc., Waltham, MA, USA) from KBr pellets in the 400–4000 cm^{-1} region.

*2.2. Synthesis of [Fe(HL)(L)]·2dmf (**1**)*

5-bromo-salicylaldehyde (0.4 g, 2 mmol) and benzhydrazide (0.27 g, 2 mmol) were dissolved in dmf (15 mL) forming a yellow solution which was magnetically stirred at 50–60 °C (30 min). Then, $FeCl_3\cdot 6H_2O$ (0.27 g, 1 mmol) was added to the hot solution of the ligand and stirred magnetically during 3 h. Dark-brown crystals suitable for X-ray analysis were formed in four days after addition of ^{i}PrOH into the resulting dark-brown solution. Yield: 0.41 g, 49%. Anal. calc. for $C_{68}H_{66}Br_4Fe_2N_{12}O_{12}$: C, 48.77; H, 3.97; N, 10.04%. Found: C, 48.75; H, 3.99; N, 10.05%. IR (KBr, cm^{-1}): 3430br, 3194w, 3062w, 2970w, 2926w, 2850w,

1680s, 1652vs, 1608vs, 1596vs, 1526s, 1492s, 1460s, 1438m, 1378vs, 1346s, 1304s, 1250w, 1182s, 1138w, 1094m, 1034w, 938w, 896w, 820m, 802m, 710s, 674m, 646m, 564m, 558w, 438w.

2.3. Crystallography

Single-crystal data for compound **1** were collected on a Gemini A diffractometer (Agilent Technologies, Santa Clara, CA, USA) equipped with an Atlas CCD detector, using graphite-monochromated MoKα radiation at 150 K. All data were processed with the CrysAlisPro 1.171.42.100a software suite [21]. Analytical absorption correction was applied to all datasets. Structure was solved using the dual-space algorithm in SHELXT-2014/7 [22], implemented in the Olex2 version 1.5 crystallographic software [23]. Independent Atom Model (IAM) refinements were performed with the SHELXL-2016/6 software [24]. Hydrogen atoms attached to carbons were placed at calculated positions and refined as riding atoms with isotropic displacement parameters. Hydrogen atom on N4 was located using a difference Fourier map, and its positional parameters were refined freely. Hirshfeld Atom Refinement (HAR) was performed using the NoSpherA2 program version 1.1.0 [16].

2.4. Crystal Data for **1**

$C_{68}H_{66}Br_4Fe_2N_{12}O_{12}$ (M = 1674.66 g mol^{-1}): triclinic, space group $P\bar{1}$ (no. 2), a = 11.0961(7) Å, b = 12.2840(6) Å, c = 13.5272(11) Å, α = 102.971(5)°, β = 101.853(6)°, γ = 99.665(5)°, V = 1713.6(2) Å^3, Z = 1, T = 149.99(10) K, μ(Mo Kα) = 2.826 mm^{-1}, D_{calc} = 1.623 g cm^{-3}, 14,368 reflections measured (4.58° ≤ 2Θ ≤ 52.738°), 6818 unique (R_{int} = 0.0376) which were used in all calculations. The final R_1 was 0.0366 ($I > 2\sigma(I)$) and wR_2 was 0.0885 (all data).

2.5. Theoretical Calculations

The ORCA 6.1.1 software package was used for all calculations [25]. Unless stated otherwise, default integration grid and loose SCF convergence criteria were applied for quantum crystallography tests, according to the default settings of NoSpherA2 [16]. The basis sets were limited to the Karlsruhe def2 family [26]. The speed-up RI or RIJCOSX approximations [27–29] and the respective def2/J auxiliary basis set [30] were applied in all cases of HAR. Optimization of H-atom positions was performed using the composite DFT method r^{2}SCAN-3c [31]. Other optimizations were performed at the ωB97X-V/def2-TZVP level. The DFT single point and CASSCF/NEVPT2 calculations were performed using tight SCF criteria, RIJK and other speed-up algorithms [32–35] and the automatic generation of auxiliary basis sets [36]. For DFT single point calculations the dispersion correction was introduced through the D4 model [37] for all functionals except of ωB97X-V. For all CASSCF/NEVPT2 (the complete active space self-consistent field with n-electron valence state second order perturbation theory) and DFT single point calculations the def2-SVP/def2-TZVPP combination of basis sets was used (def2-TZVPP basis set for iron atom and ligand atoms forming chelate cycles). The following DFT functionals have been employed in the present study: BP86 [38,39], r^{2}SCAN [40], PBE [41], PBE0 [42,43], B3LYP [44], ωB97X-V [45], TPSSh [46], and r^{2}SCAN0 [47]. The CASSCF calculations involved the super-CI approach [48]. Visualization of the molecular orbitals and 3D surfaces was performed by means of Avogadro 1.2 program [49]. All the isosurfaces are plotted at 0.02 a.u. level. Analysis and subtraction of electron densities were done using the Multiwfn 3.8 program [50]. The Cartesian xyz files of fully DFT-optimized structures of [Fe^{III}(HL)(L)] are provided in the Supplementary Information (Listing S3).

3. Results and Discussion

3.1. Synthesis and Spectroscopic Analysis

The synthetic procedure of the complex [Fe^{III}(HL)(L)]·2dmf (**1**) was divided into two steps. In the first step, the Schiff base H_2L (Scheme 1) was obtained by the condensation of 5-bromo-sastingcylaldehyde and benzhydrazide in dimethylformamide (dmf). Then, the iron(III) chloride was added to the hot yellow solution of the ligand, and the reaction was brought to completion by heating and stirring for 3 h. Dark-brown solution was obtained at the end of the reaction and dark-brown microcrystals of **1** were formed within four days after successive addition of 2-propanol (^{i}PrOH). The IR spectrum of **1** in the 4000–400 cm^{-1} range showed all the characteristic ligand peaks (Figure S1). The very strong band at 1596 cm^{-1} was assigned to ν(C=N) stretching vibrations. The presence of solvated dmf molecules was confirmed by the characteristic peak at 1680 cm^{-1}.

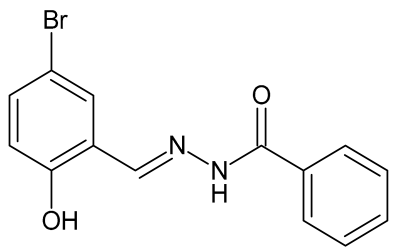

Scheme 1. Schematic representation of the ligand structure (H_2L).

3.2. Crystal Structure

The single crystal X-ray diffraction analysis of **1** disclosed its molecular structure, where two ligand molecules adopt tridentate coordination to the iron center (Figure 1, Table S1). The ligands' degree of deprotonation was found to be different, with one hydrazide group deprotonated (N2 atom). The Fe1 atom has a distorted octahedral coordination environment with the Fe–N,O bond distances ranging from 1.928(2) to 2.144(2) Å (Table S1). The hydrazide group of one of the ligands forms the strong hydrogen bond N4–H4···O5^{a} (^{a} = $1 - x$, $1 - y$, $1 - z$) to the neighboring uncoordinated dmf molecule, where d(N–H) = 0.78(4) Å, d(N···O) = 2.699(3) Å and ∠(N–H···O) = 167(4)°. The molecules of [Fe(HL)(L)] are packed to form two types of π–π stackings with interplane distances of 3.20 and 3.64 Å (Figure 2).

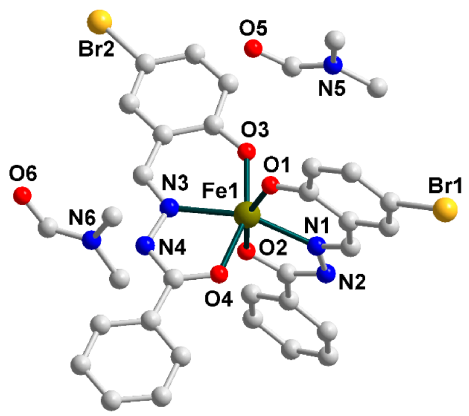

Figure 1. Molecular structure of **1** with the numbering scheme for non-carbon atoms. Hydrogen atoms are omitted for clarity. Color scheme: Fe, yellow green; Br, pale-yellow; O, red; N, blue; C, gray.

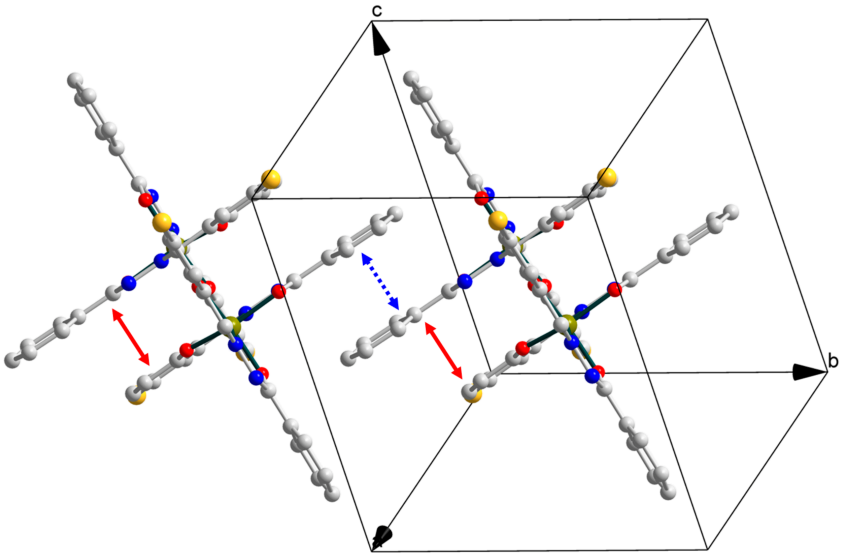

Figure 2. Fragment of the crystal structure of **1** showing π–π interactions. Solid red and blue dashed arrows indicate stacking of 3.20 and 3.64 Å distance. Hydrogen atoms and uncoordinated dmf molecules are omitted for clarity. Color scheme: Fe, yellow green; Br, pale-yellow; O, red; N, blue; C, gray.

3.3. Electronic Structure

The spin states and electronic structure were investigated using the atomic coordinates obtained from the IAM refinement. The uncoordinated dmf molecules were eliminated, and the remaining molecular structure was subjected to optimization of H-atom positions at the DFT r^{2}SCAN-3c level producing the structure [Fe^{III}(HL)(L)] (**1a**). The assumption was made that the spin structure of **1** is equal that of **1a**.

The state-averaged CASSCF/SC-NEVPT2 calculations of **1a** were performed considering all spin states averaged over 10, 10 and 4 roots for LS, IS, and HS, respectively. The (9,12) active space was constructed of five 3d Fe orbitals supported by five 4d double shell orbitals, and two ligand orbitals having the largest involvement of the metal d_{x2-y2} and d_{z2} orbitals of the iron atom (Figure 3). The CASSCF energies of the 3d Fe orbitals are in the narrow span of 2252 cm^{-1}, with the two orbitals constructed of atomic metal d_{x2-y2} and d_{z2} ones (Listing S2) having significantly higher energy that others, resulting in their lower occupancies. The occupancies of the σ-bonding counterparts (Figure 3) are close to two. However, the orbital contributing from d_{z2} (Listing S2, number 168) actively participates in the sextet excited states resulting in its lower overall occupation of 1.7 (Figure 3). The double-shell 4d iron orbitals have been included to provide flexibility of the CASSCF solutions and show close to zero occupancies, as expected. Independently on the active space composition and the number of roots, the ground state was always a single reference high-spin $S = 5/2$. The first excited state is $S = 3/2$ lying at 9164 cm^{-1} above the ground state, as obtained after SC-NEVPT2 correction (Listing S1). The lowest doublet S = 1/2 state is located at 14,249 cm^{-1}. Both the lowest quartet and doublet states appear to be of multireference nature where several Fe 3d orbitals participate as singly or doubly occupied ones. However, it is worth noting that these compositions depend much on the number of roots used for the CASSCF calculation. The results of CASSCF/NEVPT2 calculations are consistent with previously obtained experimental data on the high-spin $S = 5/2$ state of Fe(III) complexes with similar Schiff base salicylaldehyde-benzhydrazide ligands [51–53].

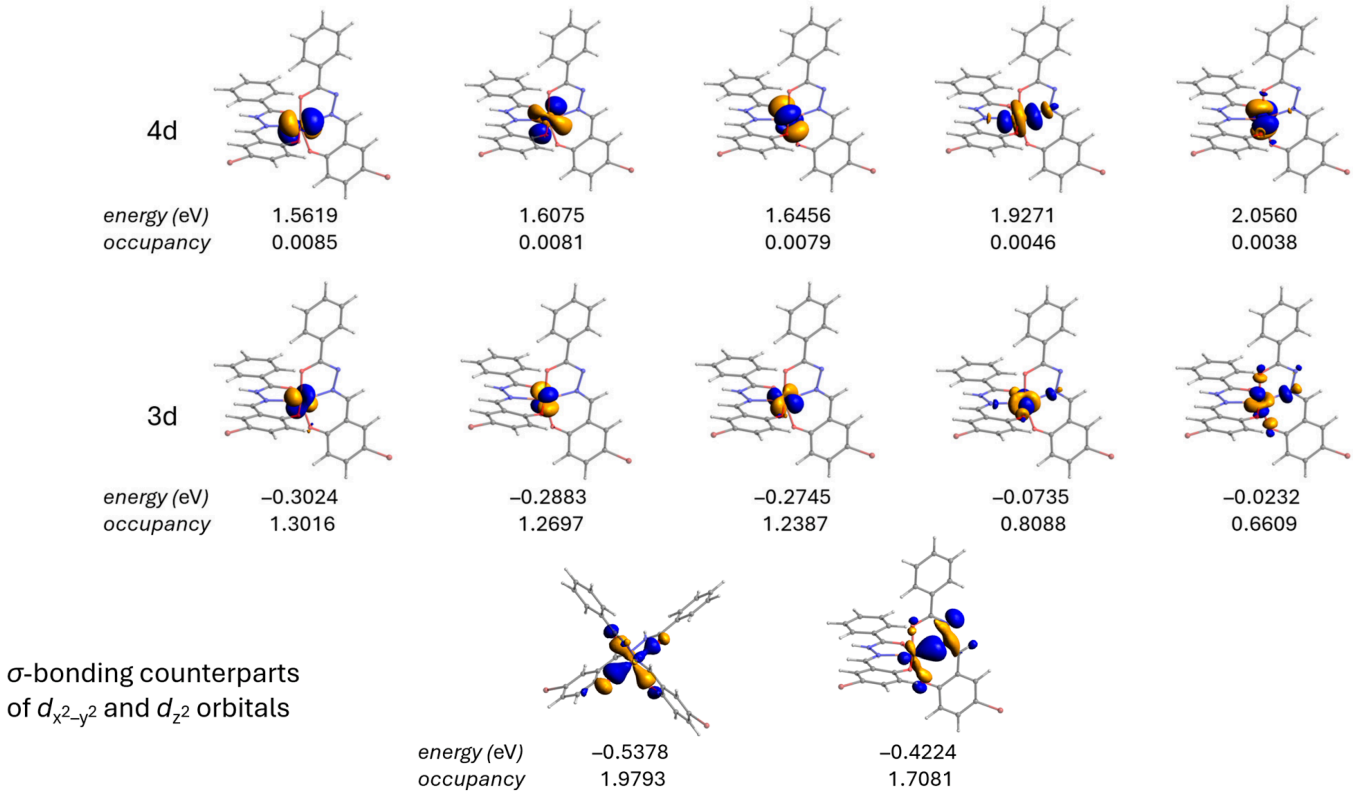

Figure 3. Isosurfaces, relative energies (eV) and occupancies of the active molecular orbitals of **1a** obtained from the CAS(9,12) calculation. 3d and 4d orbitals are those to which the corresponding atomic orbitals of iron make the greatest contribution. Positive and negative isosurfaces are plotted in blue and orange.

While the CASSCF accompanied with post-HF perturbative corrections provides explicit description of spin states of Fe(III) complexes, these methods are computationally heavy and depend much on the selected active space as well as the number of excited states. DFT, being a fast and straightforward method, is an attractive option for determining the lowest energy spin state of a Fe(III) compound. Although, by definition, the DFT deals with the single-reference ground states of a molecule, it can be applied for determination of HS–LS gaps, where the excited state is calculated assuming it is a ground state for a given multiplicity. From the variety of DFT functionals the pure ones are known to favor the LS states, while hybrid functionals overstabilize the HS states. Therefore, the DFT-calculated HS–LS gaps are strongly functional-dependent, and every case should be investigated specifically.

We calculated the energies of HS, IS and LS states of **1a** using a series of DFT functionals and compared the obtained gaps to a reference one obtained at the CASSCF/SC-NEVPT2 level, keeping in mind that high-spin $S = 5/2$ is the ground state of **1a**. As can be seen (Table S2), the non-hybrid functionals BP86 and PBE show smallest IS–HS gaps of less than 3000 cm^{-1} (compare to the reference value of 9164 cm^{-1}). The hybrid functionals TPSSh and B3LYP, as well as the pure meta-GGA r^2SCAN one, show the larger gap of ca. 6000 cm^{-1}. Finally, the largest gap of 11,000 cm^{-1} was obtained by the hybrid r^2SCAN0 functional. The LS–HS gaps maintain the same tendency. Although none of these methods can precisely determine the relative energies of spin states for **1a**, it is most important that all the functionals correctly predict the sequence of states and indicate the $S = 5/2$ as the one having lowest energy.

The spin density obtained at the CASSCF level is close to that predicted by the B3LYP calculation for the $S = 5/2$ spin state (Figure S2). The DFT difference electron (ρ^{state1}–ρ^{state2}) and spin ($\rho_S{}^{state1}$–$\rho_S{}^{state2}$) densities show that the principal changes occur on the iron atom, as expected. However, in the case of spin density the involvement of the donor atoms of ligands can also be observed (Figure 4).

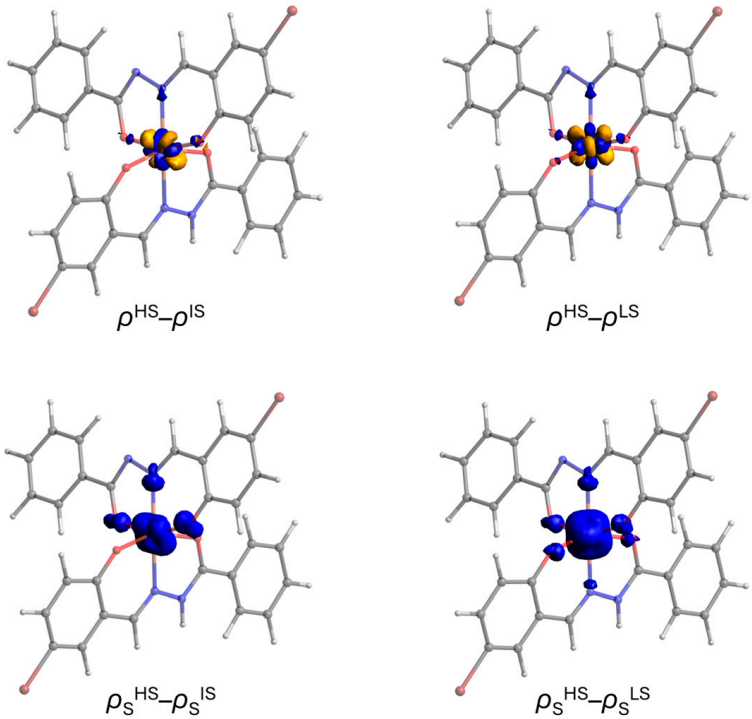

Figure 4. Isosurfaces of the difference electron (**top**) and spin (**bottom**) densities for **1a** calculated using B3LYP functional. Positive and negative isosurfaces are plotted in blue and orange.

3.4. HAR

With the knowledge of spin structure of **1** and ability of DFT functionals to describe it, we benchmarked the DFT functionals and basis sets in the Hirshfeld Atom Refinement (HAR) of the crystal structure of **1** using the NoSpherA2 program incorporated in the Olex2 package. The refinement was limited to ten cycles where electronic structures and aspheric scattering factors were recalculated in every cycle. The wR_2 indicator was used as the principal parameter to monitor the refinement quality. The weighting scheme was updated after every cycle as well. Anisotropic refinement of hydrogen atoms was applied in certain cases, keeping the riding model for H-atom coordinates. The choice of DFT functionals was governed by their direct implementation in the current version of the Olex2.NoSpherA2 software [16]. The selected functionals are commonly used in computational chemistry and cover the GGA (BP86 and PBE), meta-GGA (r^2SCAN), hybrid GGA (B3LYP and PBE0), hybrid meta-GGA (TPSSh and r^2SCAN0) and range-separated GGA (ωB97X-V) classes.

The wR_2 factors obtained for **1** by SHELXL and olex2.refine engines using the Independent Atom Model (IAM) constitute 8.85 and 8.82%, respectively. The F_o-F_c difference Fourier map reveals groups of peaks and holes around the bromine atoms Br1 and Br2, as well as the peak close to the phenyl ring of one of the ligands (Figure S3). These groups of difference densities cannot be explained by chemical reasons and hence are due to the defects of a lattice of a given crystal. In contrast, the clumps of positive density located between atoms are clearly associated with the Fe–N, N–N and other bonds, in this way being directly observable through the IAM refinement.

The HAR using the double-zeta def2-SVP basis set, anisotropic H-atom treatment and high-spin state set afforded a notable drop of wR_2 factor down to 7.51%, as observed for BP86, r^{2}SCAN and PBE0 functionals. Surprisingly, the range-separated functional ωB97X-V resulted in the highest wR_2. The increase in the basis set size up to def2-TZVP resulted in the further drop of wR_2 for the above group of functionals, but showing little changes for all others in the test. The further increase up to def2-TZVPP gives only marginal changes to wR_2 values. Independently on combination of the basis set and DFT functional, the HAR results in disappearance of the positive density in the difference Fourier map in the positions expected for interatomic bondings (Figure S3). The difference density around the iron atom is reduced only partially.

The overall results obtained for HAR for different spin states are summarized in Figure 5. As can be seen, in all cases the spin state has a notable influence on the final wR_2. The effect of a basis set is only slightly pronounced, where small and fast def2-SVP has nearly the same magnitude of ΔwR_2 as the large def2-TZVPP. The origin of the increase in *R*-factors when altering the spin state can be visually observed at the deformation Hirshfeld densities F_{IAM}–F_{HAR} calculated for all spin states (Figure 6). While the respective map of the correct HS state shows minimal changes around the iron atom introduced by the HAR model, the IS and LS states predict much stronger alterations caused by different disposition of valence electrons. The Laplacian of the electron density shown in the same plane (Figure S4) demonstrates the changes in density corresponding to those observed in Figure 6.

		BP86	r^{2}SCAN	PBE	PBE0	B3LYP	wB97X-V	TPSSh	r^{2}SCAN0
S = 5/2	def2-SVP	7.51	7.51	7.54	7.51	7.52	7.58	7.53	7.57
S = 5/2	def2-TZVP	7.48	7.47	7.49	7.53	7.54	7.54	7.55	7.53
S = 5/2	def2-TZVPP	7.49	7.47	7.49	7.53	7.54	7.54	7.54	7.53
S = 3/2	def2-TZVPP	7.57	7.56	7.52	7.56	7.57	7.57	7.58	7.55
S = 1/2	def2-TZVPP	7.55	7.52	7.56	7.58	7.61	7.59	7.54	7.56
S = 3/2	def2-SVP	7.57	7.60	7.51	7.59	7.61	7.60	7.62	7.57
S = 1/2	def2-SVP	7.58	7.56	7.60	7.56	7.58	7.64	7.59	7.60

Figure 5. wR_2 factors obtained after the HAR of **1** using given combination of DFT functional, basis set and spin state. All H-atoms were refined anisotropically.

The benchmark data summarized in Figure 5 do not indicate a systematic picture which could reveal the best DFT functional. Moreover, some functionals result in the wR_2 values of the LS state lower than that for the IS one. Given that the refined structure of 1 contains rather large peaks in the difference Fourier map located close to the hydrogen atoms H11 and H12, we investigated if the above effect can be caused by the unstable description of anisotropic H-atoms refinement in the present case. Indeed, the HAR using the spherical riding model for all hydrogen atoms gives a regular picture where in all cases the sequence wR_2 (HS) < wR_2 (IS) < wR_2 (LS) is preserved (Figure 7). The double zeta basis set was found to be sufficient for HAR determining the ground spin state of Fe(III), where the choice of the DFT functional is mostly irrelevant.

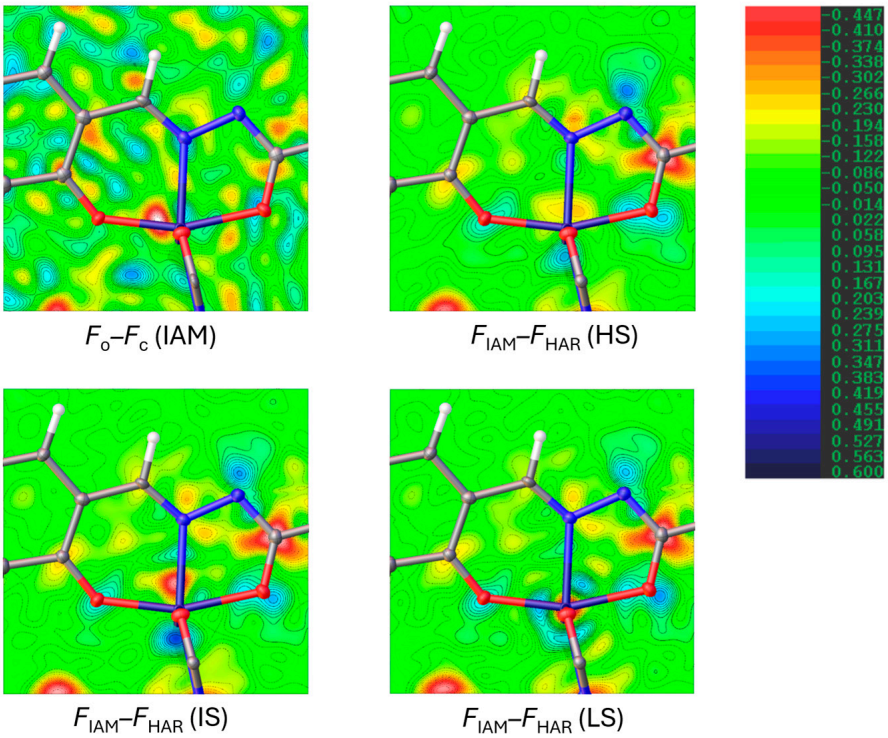

Figure 6. Plane view of the difference (IAM, olex2.refine) and deformation (NoSpherA2, B3LYP/def2-TZVPP) densities showing the region around Fe1 atom in detail. Blue and red colors correspond to positive and negative values of difference electron density $e^-/Å^3$, as indicated on the inset. Contour lines are isolevels of electron density (30 contours were used).

		BP86	r^2SCAN	PBE	PBE0	B3LYP	wB97X-V	TPSSh	r^2SCAN0
S = 5/2	def2-SVP	7.90	7.91	7.88	7.92	7.91	7.94	7.95	7.90
S = 3/2	def2-SVP	7.93	7.94	7.92	7.95	7.97	7.95	8.00	7.96
S = 1/2	def2-SVP	7.95	7.96	7.94	7.95	7.99	7.99	8.01	7.97

Figure 7. wR_2 factors obtained after the HAR of **1** using given combination of DFT functional and spin state, keeping the spherical refinement for hydrogen atoms.

DFT optimization of **1a** performed at the ωB97X-V/def2-TZVP level for different spin states (Table S3, Listing S1) indicates that the Fe–O(N) distances undergo changes in ca. 0.1 Å magnitude when changing the multiplicity. The experimental bond distances correspond to those calculated for sextet state $S = 5/2$ (Table S3), being consistent with the HAR results. Therefore, the comparison of calculated and experimental Fe–O(N) bond distances provides an additional verification instrument towards establishment of the ground spin state, and its use is recommended in appropriate cases.

The crystallographic data quality may have crucial implications on the reliability of spin state determination through the HAR method. Recently, Grabowsky and co-authors formulated the general requirements to the measured experimental data, among them absence of twinning or disorder, low R_{int} value (below 5%), high data intensity ($I/\sigma(I) > 10$ averaged and $I/\sigma(I) > 3$ for highest resolution) and other parameters [54]. Despite the presence of rather large residual difference peaks, the crystal structure of **1** meets these requirements (Figure S5), allowing for successful determination of the iron spin state through the HAR method.

4. Conclusions

In this work we have synthesized a novel coordination compound [Fe^{III}(HL)(L)]·2dmf (**1**) containing the Schiff base ligand constructed from 5-bromo-salicylaldehyde and benzhydrazide. The single crystal X-ray diffraction analysis of **1** revealed its molecular structure, where uncoordinated dmf molecules occupy voids of the lattice. Theoretical CASSCF and DFT calculations revealed the distinct high spin $S = 5/2$ ground state of **1**. The aspherical Hirsfeld atom refinement allowed for dropping the *R*-factors of the final structure and making hydrogen atoms anisotropic. We investigated the possibility of mixed theoretical–experimental determination of the spin state of Fe(III) in **1** through the methods of quantum crystallography. The results of benchmarking the DFT functionals and basis sets suggest that the double-zeta def2-SVP basis set combined with the normal integration grids and loose SCF convergence criteria are sufficient for clear determination of the spin state of iron monitored through the *R*-factors. While different DFT functionals show *R*-factors varying in a certain range, the overall sequence of *R*-factors was irrelevant to the functional. Therefore, even the fastest BP86/def2-SVP or PBE/def2-SVP combinations were found to be sufficiently precise in the case of **1**. This observation expands the practical accessibility of the HAR method for determination of spin states, since the computational costs of a calculation based on a GGA (Generalized Gradient Approximation) functional combined with a double-zeta basis set and normal integration girds are sufficiently low to be performed even on a laptop computer for a mid-size molecule of less than 100 atoms. We also stress that the observed differences in ωR^2 values are of relatively low magnitude, and thus one should be careful when making conclusions from a single calculation. One can recommend repeating it using different conditions (e.g., DFT functionals) to ensure that the obtained solution and ground state are correct. Importantly, the anisotropic H-atom refinement has led to misleading results as it increased the uncertainty of *R*-factor determination. As a final remark, herein we benchmarked only the Karlsruhe family of basis sets as the ones having a balanced efficiency and accuracy for general DFT calculations. The Pople, LANL, Jensen and other families may present different behavior which may be not directly consistent with the present conclusions.

While this study focuses on the exact high-spin Fe(III) complex, one can carefully state that the respective method can be expanded to coordination compounds of other metals, including those persisting in low or intermediate spin states at given conditions. In such cases the experimental single crystal diffraction data should be collected considering the possibility of changing the spin state with the temperature (the spin-crossover effect), and thus the data collection temperature appears to be a critically important experimental parameter which should be chosen with great care.

Supplementary Materials: The following supporting information can be downloaded at https://www.mdpi.com/article/10.3390/compounds6030047/s1, Figure S1: IR spectrum of **1**. Figure S2: Isosurfaces of spin densities calculated for **1a** by CASSCF and DFT (B3LYP). Figure S3: Isosurfaces of the difference Fo–Fc electron density calculated using olex2.refine (IAM) and NoSpherA2 (HAR, B3LYP/def2-TZVPP). Figure S4: Plots of the Laplacian of the electron density in the real space, $\nabla^2\rho(\mathbf{r})$, calculated at the B3LYP level, highlighting the difference between electron density around the iron atom in **1a**. The plane orientation corresponds to that in Figure 6. Figure S5: The plots of $I/\sigma(I)$ ratio and number of unique reflections on resolution of the source X-ray crystallographic data for **1**. Table S1: Selected bond distances (Å) and angles (°) for the crystal structure of **1**. Table S2: Absolute (top, Hartree) and relative to $S = 5/2$ sextet state (bottom, cm^{-1}) single point energies of **1a** calculated using given DFT functional and multiplicity combination. Table S3. Averaged DFT optimized and experimental Fe–O(N) bond distances (Å) of [Fe^{III}(HL)(L)] and **1**. Listing S1: Fragment of the ORCA output showing the relative states energies obtained from the CAS(9,12)/NEVPT2 calculation for **1a**. Listing S2: Adapted fragment of the ORCA output showing the relative energies

(eV) and occupancies of the active space molecular orbitals obtained from the CAS(9,12) calculation for **1a**. The rows correspond to σ-bonding orbitals number 167 and 168, 3d (169–173) and 4d (174–178) orbitals associated to iron atom, respectively. The other numbers indicate the contribution (in %) of the atomic orbitals to the respective molecular orbitals. Listing S3: Cartesian coordinates of the structures [Fe^{III}(HL)(L)] optimized at different spin states (ωB97X-V/def2-TZVP level).

Author Contributions: Conceptualization, O.V.N. and D.S.N.; methodology, D.S.N. and E.G.; formal analysis, E.A.B. and O.V.N.; investigation, E.G., E.A.B. and D.S.N.; resources, O.V.N. and E.G.; data curation, D.S.N. and O.V.N.; writing—original draft preparation, D.S.N., E.A.B. and E.G.; writing—review and editing, D.S.N. and O.V.N.; visualization, D.S.N.; supervision, O.V.N.; funding acquisition, E.A.B. and D.S.N. All authors have read and agreed to the published version of the manuscript.

Funding: This work was supported by the by the Ministry of Education and Science of Ukraine (grant No. 26BF037-01) and by the Foundation for Science and Technology (FCT, Portugal), CQE projects UID/00100/2025 (DOI https://doi.org/10.54499/UID/00100/2025), UID/PRR/00100/2025 (DOI https://doi.org/10.54499/UID/PRR/00100/2025), UID/PRR2/00100/2025 (DOI https://doi.org/10.54499/UID/PRR2/00100/2025) and IMS project LA/P/0056/2020 (DOI https://doi.org/10.54499/LA/P/0056/2020). D.S.N. thanks FCT for individual funding support through the contract 2023.15700.TENURE.014. E.G. gratefully acknowledge the Slovenian Research and Innovation Agency (ARIS) for financial support of the present study within the research program P1-0045 (Inorganic Chemistry and Technology).

Data Availability Statement: The original contributions presented in this study are included in the article/Supplementary Material. Further inquiries can be directed to the corresponding author.

Conflicts of Interest: The authors declare no conflicts of interest.

References

1. Nayek, A.; Lalaoui, N.; Duboc, C. First row transition metal dinuclear complexes for H_2 production and CO_2 reduction: From homogeneous to heterogeneous conditions. *Coord. Chem. Rev.* **2026**, *566*, 218063. [CrossRef]
2. Pointis, R.; Reynes, O.; Bastin, S.; Evrard, D.; Sortais, J.B. Hydrogenation of carboxylic acid derivatives catalyzed by 3d transition metals. *Coord. Chem. Rev.* **2026**, *560*, 217876. [CrossRef]
3. Gandeepan, P.; Muller, T.; Zell, D.; Cera, G.; Warratz, S.; Ackermann, L. 3d Transition Metals for C-H Activation. *Chem. Rev.* **2019**, *119*, 2192–2452. [CrossRef] [PubMed]
4. Singh, A.; Spiccia, L. Water oxidation catalysts based on abundant 1st row transition metals. *Coord. Chem. Rev.* **2013**, *257*, 2607–2622. [CrossRef]
5. Zhang, Y.J.; Torres-Cavanillas, R.; Yan, X.X.; Zeng, Y.X.; Jiang, M.Y.; Clemente-León, M.; Coronado, E.; Shi, S.W. Spin crossover iron complexes with spin transition near room temperature based on nitrogen ligands containing aromatic rings: From molecular design to functional devices. *Chem. Soc. Rev.* **2024**, *53*, 8764–8789. [CrossRef] [PubMed]
6. Chen, Y.X.; Ge, A.W.; Guo, X.; Yu, M.; Tao, J. Spin State Modulation Strategies for Transition Metal-Based MRI Contrast Agents. *Chem. Biomed. Imaging* **2026**, *4*, 274–303. [CrossRef] [PubMed]
7. Swart, M. Accurate Spin-State Energies for Iron Complexes. *J. Chem. Theor. Comput.* **2008**, *4*, 2057–2066. [CrossRef] [PubMed]
8. Vidal, D.; Cirera, J.; Ribas-Arino, J. Accurate calculation of spin-state energy gaps in Fe(iii) spin-crossover systems using density functional methods. *Dalton Trans.* **2021**, *50*, 17635–17642. [CrossRef] [PubMed]
9. Dey, M.; Ray, A.K.; Austen, V.; Phung, Q.M.; Yanai, T.; Paul, A.; Ghosh, D. High-quality quantum chemical data for spin state determination in transition-metal complexes. *Phys. Chem. Chem. Phys.* **2026**, *28*, 6470–6482. [CrossRef] [PubMed]
10. Schremmer, C.; Kupper, C.; Klawitter, I.; Bergner, M.; Schiewer, C.E.; Dechert, S.; Demeshko, S.; John, M.; Meyer, F. Spin-State Variations of Iron(III) Complexes with Tetracarbene Macrocycles. *Chem. Eur. J.* **2019**, *25*, 3918–3929. [CrossRef] [PubMed]
11. Kelly, C.T.; Griffin, M.; Esien, K.; Felton, S.; Muller-Bunz, H.; Morgan, G.G. Crystallographic Detection of the Spin State in FeIII Complexes. *Cryst. Growth Des.* **2022**, *22*, 6429–6439. [CrossRef] [PubMed]
12. Kelly, C.T.; Cuza, E.; Pasquetti, E.; Quinn, N.; Griffin, M.; Nockemann, P.; Müller-Bunz, H.; Bruno-Colmenarez, J.; Felton, S.; Lada, Z.G.; et al. Symmetric and asymmetric ligands for Fe^{III} spin crossover—The influence of the C_2 axis. *Dalton Trans.* **2025**, *54*, 14522–14532. [CrossRef] [PubMed]
13. Lübben, J.; Wandtke, C.M.; Hübschle, C.B.; Ruf, M.; Sheldrick, G.M.; Dittrich, B. Aspherical scattering factors for SHELXL—Model, implementation and application. *Acta Crystallogr. A* **2019**, *75*, 50–62. [CrossRef] [PubMed]
14. Grabowsky, S.; Genoni, A.; Bürgi, H.B. Quantum crystallography. *Chem. Sci.* **2017**, *8*, 4159–4176. [CrossRef] [PubMed]

15. Capelli, S.C.; Bürgi, H.B.; Dittrich, B.; Grabowsky, S.; Jayatilaka, D. Hirshfeld atom refinement. *IUCrJ* **2014**, *1*, 361–379. [CrossRef] [PubMed]
16. Kleemiss, F.; Dolomanov, O.V.; Bodensteiner, M.; Peyerimhoff, N.; Midgley, L.; Bourhis, L.J.; Genoni, A.; Malaspina, L.A.; Jayatilaka, D.; Spencer, J.L.; et al. Accurate crystal structures and chemical properties from NoSpherA2. *Chem. Sci.* **2021**, *12*, 1675–1692. [CrossRef] [PubMed]
17. Singh, A.; Pradhan, A.K.; Thomas, S.P. The Nature of One-Electron σ-Bonds Probed by X-Ray Quantum Crystallography. *ChemPhysChem* **2026**, *27*, e70441. [CrossRef] [PubMed]
18. Wenger, J.S.; Weng, M.; George, G.N.; Johnstone, T.C. Isolation, bonding and reactivity of a monomeric stibine oxide. *Nat. Chem.* **2023**, *15*, 633–640. [CrossRef] [PubMed]
19. Boronski, J.T.; Crumpton, A.E.; Wales, L.L.; Aldridge, S. Diberyllocene, a stable compound of Be(I) with a Be-Be bond. *Science* **2023**, *380*, 1147–1149. [CrossRef] [PubMed]
20. Brüx, D.; Ebel, B.; Pelzer, N.; Kalf, I.; Kleemiss, F. Experimental Spin State Determination of Iron(II) Complexes by Hirshfeld Atom Refinement. *Chem. Eur. J.* **2025**, *31*, e202404017. [CrossRef] [PubMed]
21. Oxford Diffraction. In *CrysAlisPRO*; Oxford Diffraction Ltd.: Oxfordshire, UK, 2024.
22. Sheldrick, G.M. SHELXT—Integrated space-group and crystal-structure determination. *Acta Cryst. A* **2015**, *71*, 3–8. [CrossRef] [PubMed]
23. Dolomanov, O.V.; Bourhis, L.J.; Gildea, R.J.; Howard, J.A.K.; Puschmann, H. OLEX2: A complete structure solution, refinement and analysis program. *J. Appl. Crystallogr.* **2009**, *42*, 339–341. [CrossRef]
24. Sheldrick, G.M. Crystal structure refinement with SHELXL. *Acta Cryst. C* **2015**, *71*, 3–8. [CrossRef] [PubMed]
25. Neese, F. Software Update: The ORCA Program System-Version 6.0. *Wiley Interdiscip. Rev. Comput. Mol. Sci.* **2025**, *15*, e70019. [CrossRef]
26. Weigend, F.; Ahlrichs, R. Balanced basis sets of split valence, triple zeta valence and quadruple zeta valence quality for H to Rn: Design and assessment of accuracy. *Phys. Chem. Chem. Phys.* **2005**, *7*, 3297–3305. [CrossRef] [PubMed]
27. Neese, F. An improvement of the resolution of the identity approximation for the formation of the Coulomb matrix. *J. Comput. Chem.* **2003**, *24*, 1740–1747. [CrossRef] [PubMed]
28. Neese, F.; Wennmohs, F.; Hansen, A.; Becker, U. Efficient, approximate and parallel Hartree-Fock and hybrid DFT calculations. A 'chain-of-spheres' algorithm for the Hartree-Fock exchange. *Chem. Phys.* **2009**, *356*, 98–109. [CrossRef]
29. Helmich-Paris, B.; de Souza, B.; Neese, F.; Izsak, R. An improved chain of spheres for exchange algorithm. *J. Chem. Phys.* **2021**, *155*, 104109. [CrossRef] [PubMed]
30. Weigend, F. Accurate Coulomb-fitting basis sets for H to Rn. *Phys. Chem. Chem. Phys.* **2006**, *8*, 1057–1065. [CrossRef] [PubMed]
31. Grimme, S.; Hansen, A.; Ehlert, S.; Mewes, J.M. r^2SCAN-3c: A "Swiss army knife" composite electronic-structure method. *J. Chem. Phys.* **2021**, *154*, 064103. [CrossRef] [PubMed]
32. Kossmann, S.; Neese, F. Comparison of two efficient approximate Hartee-Fock approaches. *Chem. Phys. Lett.* **2009**, *481*, 240–243. [CrossRef]
33. Guo, Y.; Sivalingam, K.; Neese, F. Approximations of density matrices in N-electron valence state second-order perturbation theory (NEVPT2). I. Revisiting the NEVPT2 construction. *J. Chem. Phys.* **2021**, *154*, 214111. [CrossRef] [PubMed]
34. Kollmar, C.; Sivalingam, K.; Guo, Y.; Neese, F. An efficient implementation of the NEVPT2 and CASPT2 methods avoiding higher-order density matrices. *J. Chem. Phys.* **2021**, *155*, 234104. [CrossRef] [PubMed]
35. Ugandi, M.; Roemelt, M. A recursive formulation of one-electron coupling coefficients for spin-adapted configuration interaction calculations featuring many unpaired electrons. *Int. J. Quant. Chem.* **2023**, *123*, e27045. [CrossRef]
36. Stoychev, G.L.; Auer, A.A.; Neese, F. Automatic Generation of Auxiliary Basis Sets. *J. Chem. Theor. Comput.* **2017**, *13*, 554–562. [CrossRef] [PubMed]
37. Caldeweyher, E.; Ehlert, S.; Hansen, A.; Neugebauer, H.; Spicher, S.; Bannwarth, C.; Grimme, S. A generally applicable atomic-charge dependent London dispersion correction. *J. Chem. Phys.* **2019**, *150*, 154122. [CrossRef] [PubMed]
38. Becke, A.D. Density-functional exchange-energy approximation with correct asymptotic-behavior. *Phys. Rev. A* **1988**, *38*, 3098–3100. [CrossRef] [PubMed]
39. Perdew, J.P. Density-functional approximation for the correlation-energy of the inhomogeneous electron-gas. *Phys. Rev. B* **1986**, *33*, 8822–8824. [CrossRef] [PubMed]
40. Furness, J.W.; Kaplan, A.D.; Ning, J.L.; Perdew, J.P.; Sun, J.W. Accurate and Numerically Efficient r^2SCAN Meta-Generalized Gradient Approximation. *J. Phys. Chem. Lett.* **2020**, *11*, 8208–8215. [CrossRef] [PubMed]
41. Perdew, J.P.; Burke, K.; Ernzerhof, M. Generalized gradient approximation made simple. *Phys. Rev. Lett.* **1996**, *77*, 3865–3868. [CrossRef] [PubMed]
42. Adamo, C.; Barone, V. Toward reliable density functional methods without adjustable parameters: The PBE0 model. *J. Chem. Phys.* **1999**, *110*, 6158–6170. [CrossRef]

43. Ernzerhof, M.; Scuseria, G.E. Assessment of the Perdew-Burke-Ernzerhof exchange-correlation functional. *J. Chem. Phys.* **1999**, *110*, 5029–5036. [CrossRef]
44. Stephens, P.J.; Devlin, F.J.; Chabalowski, C.F.; Frisch, M.J. Ab-initio calculation of vibrational absorption and circular-dichroism spectra using density-functional force-fields. *J. Phys. Chem.* **1994**, *98*, 11623–11627. [CrossRef]
45. Mardirossian, N.; Head-Gordon, M. ωB97X-V: A 10-parameter, range-separated hybrid, generalized gradient approximation density functional with nonlocal correlation, designed by a survival-of-the-fittest strategy. *Phys. Chem. Chem. Phys.* **2014**, *16*, 9904–9924. [CrossRef] [PubMed]
46. Staroverov, V.N.; Scuseria, G.E.; Tao, J.M.; Perdew, J.P. Comparative assessment of a new nonempirical density functional: Molecules and hydrogen-bonded complexes. *J. Chem. Phys.* **2003**, *119*, 12129–12137. [CrossRef]
47. Bursch, M.; Neugebauer, H.; Ehlert, S.; Grimme, S. Dispersion corrected r^2SCAN based global hybrid functionals: r^2SCANh, r^2SCAN0, and r^2SCAN50. *J. Chem. Phys.* **2022**, *156*, 134105. [CrossRef] [PubMed]
48. Kollmar, C.; Sivalingam, K.; Helmich-Paris, B.; Angeli, C.; Neese, F. A perturbation-based super-CI approach for the orbital optimization of a CASSCF wave function. *J. Comput. Chem.* **2019**, *40*, 1463–1470. [CrossRef] [PubMed]
49. Hanwell, M.D.; Curtis, D.E.; Lonie, D.C.; Vandermeersch, T.; Zurek, E.; Hutchison, G.R. Avogadro: An advanced semantic chemical editor, visualization, and analysis platform. *J. Cheminform.* **2012**, *4*, 17. [CrossRef] [PubMed]
50. Lu, T.; Chen, F.W. Multiwfn: A multifunctional wavefunction analyzer. *J. Comput. Chem.* **2012**, *33*, 580–592. [CrossRef] [PubMed]
51. Cheaib, K.; Martel, D.; Clément, N.; Eckes, F.; Kouaho, S.; Rogez, G.; Dagorne, S.; Kurmoo, M.; Choua, S.; Welter, R. Structural, magnetic and optical properties of an Fe^{III} dimer bridged by the meridional planar divergent *N*,*N′*-bis(salicyl)hydrazide and its photo- and electro-chemistry in solution. *Dalton Trans.* **2013**, *42*, 1406–1416. [CrossRef] [PubMed]
52. Matoga, D.; Szklarzewicz, J.; Stadnicka, K.; Shongwe, M.S. Iron(III) complexes with a biologically relevant aroylhydrazone: Crystallographic evidence for coordination versatility. *Inorg. Chem.* **2007**, *46*, 9042–9044. [CrossRef] [PubMed]
53. Wang, K.; Chen, Z.L.; Zou, H.H.; Li, Y.; Liang, F.P. A series of 3d metal complexes prepared by in situ reactions of a flexible diacylhydrazine ligand: Synthesis, structures and magnetic properties. *Trans. Met. Chem.* **2017**, *42*, 17–23. [CrossRef]
54. Balmohammadi, Y.; Malaspina, L.A.; Nakamura, Y.; Cametti, G.; Siczek, M.; Grabowsky, S. A quantum crystallographic protocol for general use. *Sci. Rep.* **2025**, *15*, 13584. [CrossRef] [PubMed]

Disclaimer/Publisher's Note: The statements, opinions and data contained in all publications are solely those of the individual author(s) and contributor(s) and not of MDPI and/or the editor(s). MDPI and/or the editor(s) disclaim responsibility for any injury to people or property resulting from any ideas, methods, instructions or products referred to in the content.